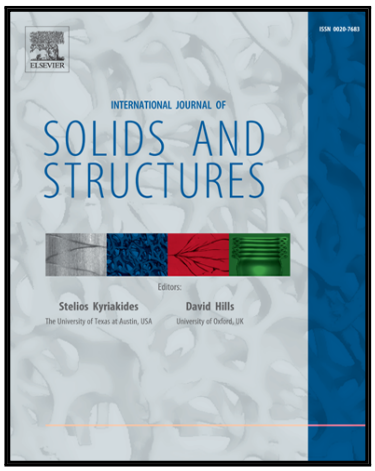

Experimental Characterization of Compaction Wave Propagation in Cellular Polymers

Suraj Ravindran , Behrad Koohbor , Peter Malchow , Addis Kidane

PII: S0020-7683(18)30050-7
DOI: 10.1016/j.ijsolstr.2018.02.003
Reference: SAS 9888

To appear in: *International Journal of Solids and Structures*

Received date: 17 May 2017
Revised date: 21 November 2017
Accepted date: 1 February 2018

Please cite this article as: Suraj Ravindran , Behrad Koohbor , Peter Malchow , Addis Kidane , Experimental Characterization of Compaction Wave Propagation in Cellular Polymers, *International Journal of Solids and Structures* (2018), doi: 10.1016/j.ijsolstr.2018.02.003

Highlights

- Equations have been modified, only the necessary equations are given
- A X-T diagram has been added
- A section, critical impact velocity to generate shock is added
- Detail information about the compaction and elastic wave propagation is given
- We went through the entire document and made necessary corrections

Experimental Characterization of Compaction Wave Propagation in Cellular Polymers

Suraj Ravindran, Behrad Koohbor, Peter Malchow, Addis Kidane[1]
Department of Mechanical Engineering, University of South Carolina, 300 Main Street, Columbia, SC 29208

Abstract

A great-deal of literatures is available in the study of compaction wave propagation in cellular materials. However, the experimental investigations concerning the spatial variation of the deformation features of compaction waves are limited. In this study, an experimental methodology based on digital image correlation (DIC) is presented to understand the formation and propagation of compaction wave in a low density polymeric foam under intermediate velocity projectile impact loading. The results are discussed in terms of the compaction wave characteristic parameters such as compaction wave velocity, axial strain, particle velocity etc. In addition, spatial distribution of inertia stress during compaction wave propagation period is obtained and evaluate of the compaction thickness is estimated for the first time. The stress jump across the compaction wave is calculated using an inertia stress analysis and compared with the shock theory. It was observed that an elastic precursor propagates, at a velocity of 740 m/s, along the material upon impact, and it decays as it propagates along the specimen. The decay of the elastic precursor could be due to the cellular scale material failure caused by micro buckling during the elastic wave propagation. The compaction wave formed followed by the elastic precursor was propagated at a constant velocity. Inertia stress calculations show the two-wave structure, the fast moving elastic precursor reflects from the distal end which reduces the inertia component of the stress. Compaction thickness is seen to be approximately constant during the entire duration of the compaction wave propagation after the achievement of the quasi-steady condition.

KEYWORDS: polymer foam; wave propagation; direct impact; digital image correlation; high speed photography

[1] Corresponding Author
Address: Department of Mechanical Engineering (Room A132), University of South Carolina, 300 Main Street, Columbia, South Carolina, 29208, USA | Email: kidanea@cec.sc.edu | Tel: +1 (803) 777 2502 | Fax: +1 (803) 777 0106

1. Introduction

High specific stiffness, strength and energy absorption characteristics of cellular solids make them an attractive class of materials for a wide range of applications, from packaging to impact damage protection (Ashby et al., 2000; Gibson and Ashby, 1999). Among various types of cellular materials, polymeric foams have shown great potentials in a variety of applications and in different loading conditions, from quasi-static to high-velocity impacts. When studying deformation response in quasi-static and low-velocity impact, polymeric foams are treated similar to non-porous non-cellular solids. However, at relatively higher strain rate conditions, there are certain challenges associated with the mechanical characterization of polymeric foams that require special experimental instruments and more complex approaches.

In impact loading, depending on the properties of the foam material and the impact velocity, compaction waves can form and propagate at a speed higher than the impact velocity (Radford et al., 2005; Reid and Peng, 1997). In order to design such materials for blast and impact damage protections, a detailed understanding of the compaction wave propagation in polymeric foams is required. The past, the characteristics of the compaction wave have been studied with the help of theoretical models, numerical method and experiments (Barnes et al., 2014; Elnasri et al., 2007; Karagiozova et al., 2012; Pattofatto et al., 2007; Reid and Peng, 1997; Zheng et al., 2005). A rate-independent rigid perfectly plastic locking model (RPPL) has been developed in order to predict the strength enhancement in wood under impact loading (Reid and Peng, 1997). This model has been further improved with the inclusion of strain hardening (Hanssen et al., 2002; Pattofatto et al., 2007). Harrigen et al.(Harrigan et al., 2005), used an elastic-perfect-plastic model with hardening while Lopatnikov et al. (Lopatnikov et al., 2003), used elastic plastic perfect rigid locking (EPPR) to predict the strength enhancement in foams. In addition, there are

shock wave models that have been formulated to determine the critical impact velocity at which the shock waves are formed in cellular materials (Sun et al., 2016; Tan et al., 2002). These models are extensively used to study the compaction wave propagation in cellular materials. To enrich the numerical and theoretical analyses of the compaction wave propagation and the deformation behavior at dynamic loading conditions, several experiment-based works have also been conducted (Song et al., 2006; Subhash et al., 2006). The experimental works have mostly used Hopkinson bar apparatus or its modified direct impact setups. One particular challenge in the use of Hopkinson bar in the study of dynamic deformation and wave propagation response in cellular materials, in general, is due to the significantly low mechanical impedance of these materials, which results in a belated state of stress equilibrium. This cause the deviation from the very basic assumption of homogenous deformation in wave analysis of strain signals from Hopkinson bar. Therefore, the length of the specimen and the impact velocity that can be used in a standard SHPB technique is limited. Also, it is seen that the impact velocity must be lower than 50 m/s in order to obtain the accurate constitutive properties when using SHPB to characterize Alulight and Duocel foams (Deshpande and Fleck, 2000). In this regard, under high impact velocity loading, when a compaction wave is formed within the sample, calculation and analysis of stress gradients across the sample may not be done in a straight forward manner. A remedy to this issue is to conduct two independent impact experiments, forward and backward impact, using which the average stress magnitudes ahead of and behind the compaction wave front can be estimated (Barnes et al., 2014; Lee, 2006; Merrett et al., 2013). Such experiments are devised with the help of force measurements at the boundaries of the sample, therefore, an *in-situ* study of the stress wave propagation in the material may not be possible. In addition, spatial variation of parameters such as particle velocity and stresses, and measurement of compaction wave

thicknesses cannot be obtained through boundary measurements. Currently, there are no experiments that can estimate the stress on either side of the compaction front, which is essential in understanding the behavior of foam under impact loading.

The advent of digital image correlation (DIC) has made it possible to measure the distribution of deformation kinematics over a well-defined boundary over a wide range of length and time scales (Ravindran et al., 2017; S Ravindran et al., 2016; Suraj Ravindran et al., 2016a, 2016b; Zhao et al., 2005). In specific case of cellular materials subjected to dynamic loading, high speed imaging in conjunction with DIC have facilitated the estimation of wave velocity at moderate impact velocities (Barnes et al., 2014; Lee, 2006). The application of high speed DIC in the study of polymeric foams under impact loading conditions has been investigated in a series of recent publications (Koohbor et al., 2016a, 2016b, 2015). Using full-field displacement and strain data obtained via stereovision DIC, Koohbor et al. (Koohbor et al., 2016c) have been able to estimate the distribution of acceleration and density in cylindrical foam specimens subjected to direct impact loading. Acceleration and density data have then been utilized to calculated temporal and spatial distribution of inertia stresses developed during impact experiments. The estimated inertia stresses have been superimposed with the boundary measured stress, enabling calculation of the full-field stress values over the entire area of interest at any given time. The approach developed for calculation of stress in this way is promising in the case of compaction wave propagation in the polymeric foams. Such analyses can enable a more in-depth analysis of wave propagation mechanisms, as well as the study of possible damping mechanisms in the material. Accordingly, our objective in this work is to develop an experimental method based on high speed DIC to characterize wave propagation behavior in low density polymer foams subjected to direct impact. The approach previously proposed for the estimation of full-field stress has been extended to

large deformation conditions in this work, using which possible damping mechanisms in the examined material are studied.

2. Material and Methods

2.1. Materials and Specimen Preparation

The material examined in this study was a closed-cell polymeric foam supplied by General Plastics Co. Nominal density of the material was measured in-house as 154±5 kg/m^3. Fig. 1 depicts the engineering stress-engineering strain response of the examined foam under compression at a nominally-constant strain rate of 10^{-3}/s. Compressive elastic modulus was determined from the slope of the linear region of the stress-strain curve as 49±4 MPa. Elastic modulus measurements were determined from three independent measurements. Poisson's ratio of the material in elastic regime is also determined by measuring the lateral and axial strains via DIC under quasi-static loading, details of which can be found elsewhere (Koohbor et al., 2015). Accordingly, the elastic Poisson's ratio is measured as υ_e=0.35±0.01 , from three independent measurements.

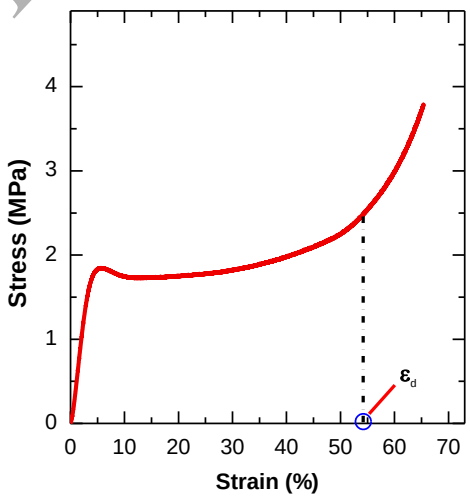

Fig. 1- Nominal stress-strain response of the examined foam under quasi-static compression.

For the dynamic experiments, rectangular specimens were extracted from a single foam billet using a band saw. The final machining of the sample to the desired dimensions was performed in a milling machine, followed by sand polishing to produce a smooth surface finish. Final dimensions of the specimen were 20×14×14 mm^3. Front surface of the specimen was prepared for DIC measurements by applying a high contrast random speckle pattern containing black and white particles with average 500 μm speckle dimensions. Speckle pattern was produced using an airbrush spray.

2.2. Experimental Setup

A modified Hopkinson bar apparatus, only using the transmitter bar, was used to apply impact loading on the specimen. As shown in Fig. 2, the specimen is placed and fixed on the left end of the transmitter bar, while direct impact is applied on the left side of the specimen. The specimen is held on the bar with the use of a lithium-based grease which serves also as a lubricant to diminish the effects due to friction. Loading system consists of a launching tube attached to a compressed gas tank (gas-gun). Compressed helium was used in the gas-gun to launch the projectile. The bore dimeter and length of launching tube were 25.4 mm and 3040 mm, respectively. The bore of the launching tube was precisely aligned with the transmitter bar in order to produce near perfect plane impact on the specimen. A projectile made of polycarbonate with 24.3 mm in diameter and 88 mm in length was used in this study. Impact face of the projectile was precisely machined and polished for a smooth impact face. The projectile was shot directly toward the specimen, the velocity of which upon impact was measured as 90 m/s. This

impact velocity, as discussed later, is high enough to produce a compaction wave in the material. It should be noted that our intention in this work was to study the deformation response of the impacted specimen over a time period during which the compaction wave traverses and reaches the distal end of the imapcted specimen. Therefore, the strain on the transmitter bar was not needed for the data analysis.

To facilitate *in-situ* full-field deformation measurements, an ultra-high speed camera HPV-X2 (Hadland Imaging) was used. The utilized high-speed camera system has the capability to record 128 images at 0.2 μs interframe time and an image resolution of 400×250 pixel^2. In the present work, in order to record the entire course of deformation from the instant of initial impact until complete densification, the maximum possible framing rate was not used, instead an interframe time of 1.5 μs was selected. The optics of the system consists of a 100 mm Tokina lens attached to the camera. The illumination was provided by the metal arc lamp (Lumen 200). An optical resolution of 100 μm/pixel was achieved with the optical system used.

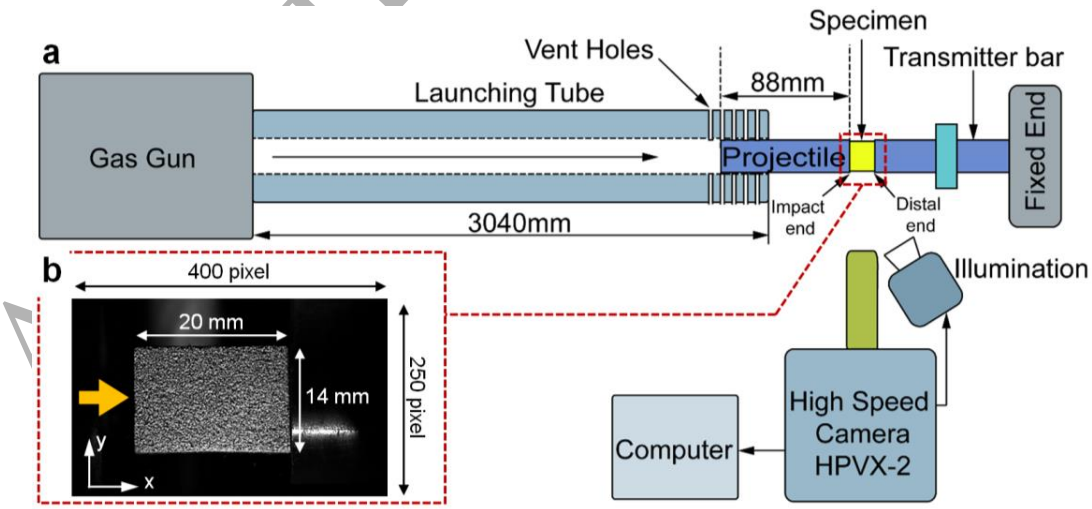

Fig. 2- (a) Schematic of the experimental setup. Camera view of the speckled specimen and the dimensions of the area of interest are shown in (b).

3. Post-Processing

3.1. Digital Image Correlation

Images acquired during the deformation time were processed in the commercial digital image correlation software Vic-2D (Correlated Solutions Inc.). Following the common rule of thumb for the selection of subset and step sizes (Sutton et al., 2009) and using the average speckle size (500 μm) as the baseline, subset and step sizes of 13×13 pixel^2 (1.3×1.3 mm^2) and 2 pixels, respectively, were used for image correlation in this work. Full-field displacements and strains were calculated through an incremental correlation mode. The incremental algorithm was used here to enable data acquisition at very high compressive strains of the order of 50%, without any significant decorrelation. A higher order interpolation function (Optimized 8-tap) was used to convert discrete digital data points to continuous data. Correlation criterion was chosen to be zero normalized, which is insensitive to the scaling of light intensity.

3.2. Full-Field Stress and Density Calculation

Our focus in this work was to utilize full-field measurement to explain the compaction wave propagation response in cellular polymers. Considering the kinematics of the deformation, displacement distribution can be obtained as the direct output of a DIC measurement. Displacement fields can be differentiated with respect to space and/or time to give the distribution of velocity, acceleration, strain and strain rate fields within the area of interest. Full-field stress distribution, on the other hand, is not a readily measurable parameter. Spatial

variability of stress during the compaction wave propagation is due to the predominance of *inertia stresses* developed in the specimen. In order to account for the inertia loading conditions existing in this study as well as to facilitate determining full-field stress and density data an extension of the approach recently implemented by the authors is adopted here (Koohbor et al., 2016c, 2015).

The density field can be calculated by using the full-field displacement data obtained from the experiment. The density of the material with time (ρ) is related to initial density as shown below,

$$J\rho = \rho_0 \tag{1}$$

Where ρ_0, is the initial density of the material and J is the Jacobian at a point at any given time t, and it is calculated as J=det F. Where, F denotes the deformation gradient and it is determined from the displacement field (d) obtained via DIC.

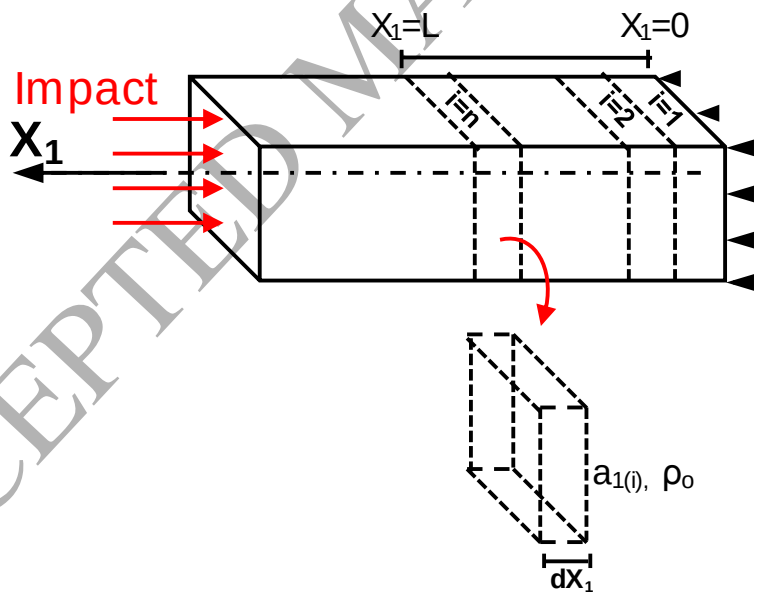

Fig. 3- Schematic view of a rectangular specimen subjected to direct impact. The right (distal) end of the specimen is fixed in X_1-direction and the impact loading is applied on the left end.

Compaction wave stress before the wave reaches the distal end of the specimen can be calculated using the acceleration field obtained from full-field displacement. A brief description of the method is outlined below. Fig. 3 schematically shows a specimen impacted by a projectile at its left end (X_1 = 0 mm). The linear momentum conservation in Lagrangian description, neglecting the body force term can be written as:

$$\nabla \bullet S = \rho_0 \frac{\partial u}{\partial t}|_{X=constant} \tag{2}$$

where S is the inertial *First Piola Kirchoff* stress and $\frac{\partial u}{\partial t}$ is the Lagrangian acceleration,

Total axial *First Piola Kirchoff* stress, $P_{11}(X_1,t) = P_{11}(0,t) + \int_0^{X_1} \rho_0 \frac{\partial u_1}{\partial t} dX_1$ (3)

From Eq.2, the axial Cauchy's stress can be obtained as:

$$\sigma_{11}(X_1,t) = \frac{P_{11}(X_1,t)}{\left[1+\frac{\partial d_2}{\partial X_2}\right]\left[1+\frac{\partial d_3}{\partial X_3}\right]} \tag{4}$$

It should be noted that Eq.3 was obtained by neglecting the shear strain and the gradients of d_1 in X_2 and X_3 direction. This is a reasonable assumption, as the shear strain developed in the low-density foam under impact loading is negligible, as the deformation is mostly constrained in one direction. This is discussed in section 4.1. In addition, $P_{11}(0,t)$ =0 before the wave reaches the distal end of the sample.

According to Eqs. 3 and 4, axial acceleration and the displacement components are required to calculate the axial Cauchy's stress. The displacement component (d_2) can be directly obtained from DIC and d_3 is assumed to be equal to d_2. Distribution of axial acceleration in time and space

can be simply obtained by applying a three-term finite difference operator onto the axial displacement data extracted from DIC as:

$$a_1(X_1,t)=\frac{1}{\Delta t^2}\left[d_1(X_1,t-\Delta t)-2d_1(X_1,t)+d_1(X_1,t+\Delta t)\right] \quad (5)$$

where d_1 and Δt denote axial displacement component and interframe time (=1.5 μs), respectively.

4. Results and Discussion

4.1. In-Situ Strain Measurements and Density

Deformation response of the foam was captured and analyzed via 2D DIC. Fig. 4 shows selected gray level images used for image correlation analysis. A qualitative evaluation of these gray level images indicates an insignificant lateral deformation, confirming the predominance of uniaxial bulk deformation state during the record time. In addition, gray level images show no evidence of defocusing and/or blurring effects, which is due to a negligible out-of-plane deformation.

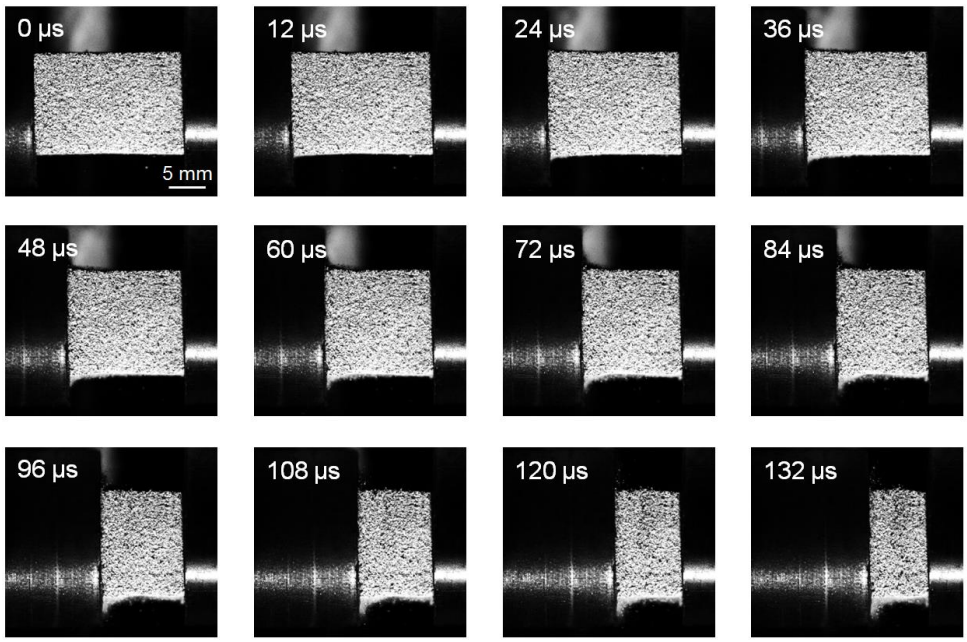

Fig. 4-Gray level images recorded during deformation of the specimen. The reference time (t = 0 μs) indicates the instant when impactor first contacts the specimen.

Before going any further into the deformation analysis, it should be noted that the full-field data was obtained in this work over an area slightly smaller than the entire speckled area (see Fig. 5). This is in fact due to the intrinsic nature of DIC algorithm which requires data extraction from the center of subsets. As a result, a narrow strip of data with a width equal to half of the subset size will be lost around the edges of the original speckled area. This issue has been previously addressed by either reducing the subset size, or extrapolating the 2D data maps to reconstruct the missing data near the edges (Wang et al., 2013). The former remedy requires finer speckle patterns while reducing the subset size essentially increases the noise level. The latter remedy also requires extensive data analysis and is beyond the scope of this work. Therefore, our area of interest in this work will be basically 1.3 mm (2×0.65 mm) smaller than the entire speckled area. Accordingly, the impacted and distal ends of the specimen hereafter will be referred to the edges of the DIC area of interest, and not the actual physical boundaries of the specimen.

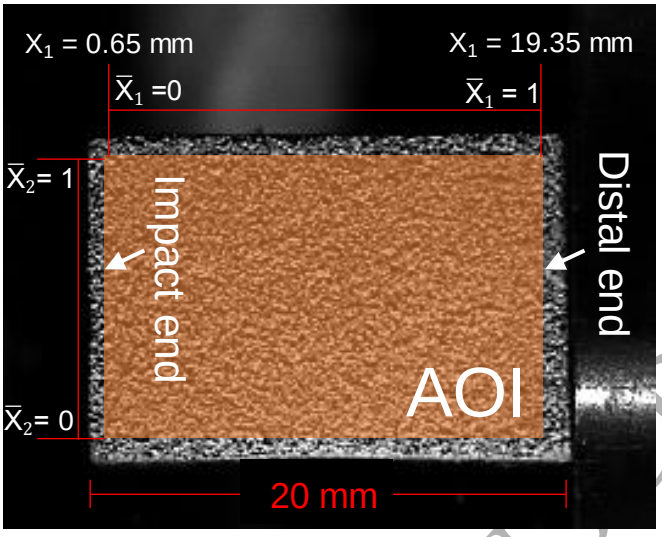

Fig. 5- View of the speckled and full-field measurement areas. AOI denotes the area over which data extraction and analysis were performed.

Displacement and strain fields were obtained over the area of interest. Contour maps showing the evolution of axial strain are shown in Fig. 6. Note that due to the large deformation nature of the experiments in this work, the dimensions of the area of interest constantly reduce with deformation time. This was shown earlier in Fig. 4. To avoid any further confusion, the contour maps shown in Fig. 6 were all plotted in undeformed coordinates, i.e. in the normalized coordinates detailed in Fig. 5. It is clearly seen that a high strain region is formed upon the first establishment of the contact between the specimen and the impactor. This high strain band then propagates toward the distal end of the specimen, consuming the entire area of interest in approximately 108 μs. Distribution of axial strain shows strong spatial heterogeneities within the area of interest, a typical behavior shown by other cellular materials under dynamic deformation conditions, as well (Barnes et al., 2014). Vertical iso-strain contour lines confirm the predominance of uniaxial deformation and negligible shear deformation. Contour lines are shown to be slightly deviated from a perfect vertical pattern after t =72 μs. Negligible shear-type

deformation here might be due to either slight misalignments between the fixed support and the specimen end, or simply the local density inconsistency within the specimen, causing variations in the local material response. Note that after t =120 μs, there are points near the impact end that show decorrelation due to excessive deformation. These points are marked with dashed circles on the contour maps in Fig. 6.

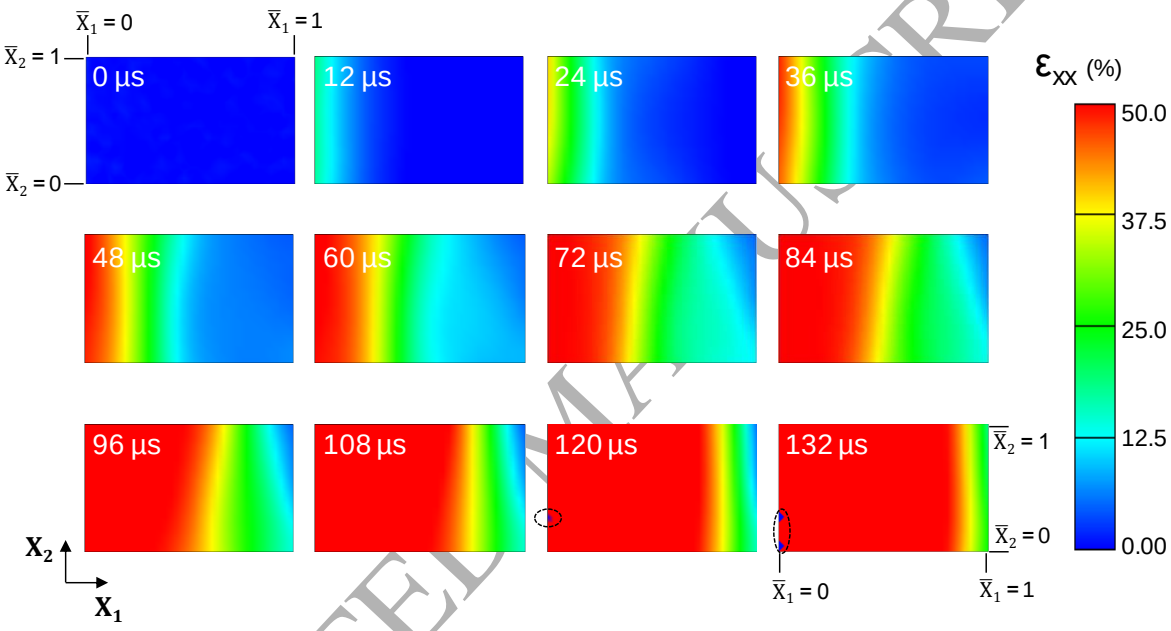

Fig. 6- Full-field axial engineering strain at different times showing the propagation of the compaction band front along the specimen axis.

Fig. 7a shows typical variation of strain components in time extracted from a representative point located on the impacted end of the specimen. Considering Fig. 7a, there are two points worth mentioning: (1) maximum shear strain magnitudes, ε_{xy}, developed in the material are shown to be less than 0.025. This type of behavior was found to be consistent throughout the entire area of interest and at all times, and confirmed the presence of insignificant shear deformation. (2) The

lateral strain history, ε_{yy}, shows no particular increase during the first 60 μs after the impact, i.e. time duration required for the complete compaction of the foam at the impacted end of the specimen. The material undergoes near-perfect uniaxial deformation state. The Poisson's effect during this time is minimal and Poisson's ratio is very close to zero. At t = 60 μs, the local axial strain value developed at the impact end of the specimen reaches the densification strain, a fully-densified band is formed over this region and consequently, the material loses capability of any further densification. The fully-densified region behind the compaction wave behaves more like a solid material, while the deformation state over this region switches to uniaxial stress. During this time, the lateral strain starts to build up and the Poisson's ratio will no longer be zero, but remains under 0.1 until the deformation end. A negligible Poisson's ratio indicates a very negligible gradient of displacement d_2 and d_3 in X_2 and X_3 direction respectively. Due to the complexities in the deformation response of the material behind and ahead of compaction wave, particularly in terms of strain and stress states, we will hereafter focus on the deformation of a thin strip of data positioned horizontally along the $\overline{X}_2$=0.5 line (see Fig. 5).

Instantaneous density is an important parameter in compaction and it determines the strength of compaction wave. Spatial and temporal variations of nominal density were calculated using Eq. 1. Fig. 7b illustrates curves showing the variations in nominal density at various times. Note the density calculations are conducted over the thin data strip expanded along the mid-width of the area of interest. The initial density of the material is taken as the average bulk density value measured prior to the experiment, i.e. ρ_0 =154 kg/m^3. Consistent with the discussions provided earlier on the deformation response of the material, density data show an initial increase occurred on the impacted side for approximately 60 μs after the impact. Afterwards, nominal density on the fully-densified impacted side of the specimen remains almost constant, while the compaction

band propagates along the specimen axis and densifies the rest of the specimen. It is worth noting that density increase of more than 180% is calculated for the specimen in this work. Such significant density increase is expected owing to the relatively low initial density (high porosity) of the examined foam, as well as the fact that the deformation is highly constrained in one-dimension only due to lateral inertia confinement.

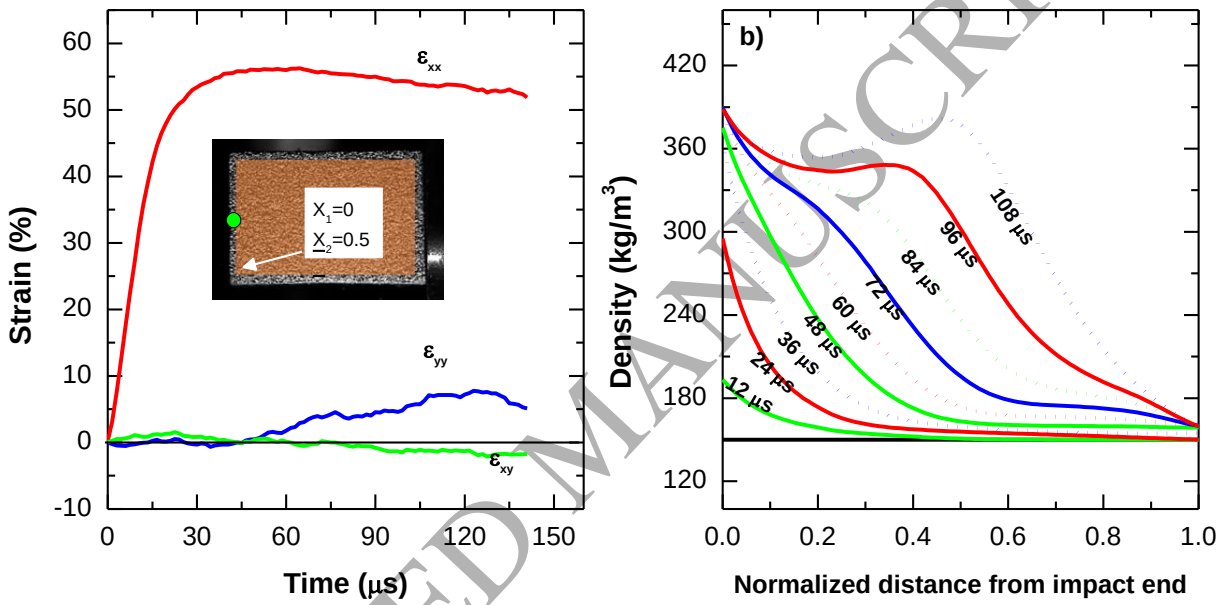

Fig. 7- (a) Curves showing the evolution of various strain components extracted from a point at the impacted point of the specimen. (b) Spatial variation of nominal density in time, calculated based on Eq. 1. Results are obtained along $\bar{X}_2 = 0.5$.

4.2. Particle Velocity and Wave Speed

Fig. 8 illustrates the distribution of particle velocity in X_1-direction. The maximum particle velocity is shown to remain constant at all times with its value equal to the impactor velocity. The location of the compaction wave front is depicted in Fig. 8 by a signifincat gradient in the velocity, as will be discussed in more details later. Note that the compaction wave front remains nearly planar during the entire duration of the deformation. Another interesting point in the

contour maps is that particle velocity patterns ahead of compaction wave front do not show a planar distribution and instead indicate a symmetrical distribution about the center line ($\overline{X}_2 = 0.5$). This behavior is particularly evident in the contour maps plotted at t =24 μs and t =36 μs, and can be attributed to the effects of free surface boundary on the elastic wave propagation in the material.

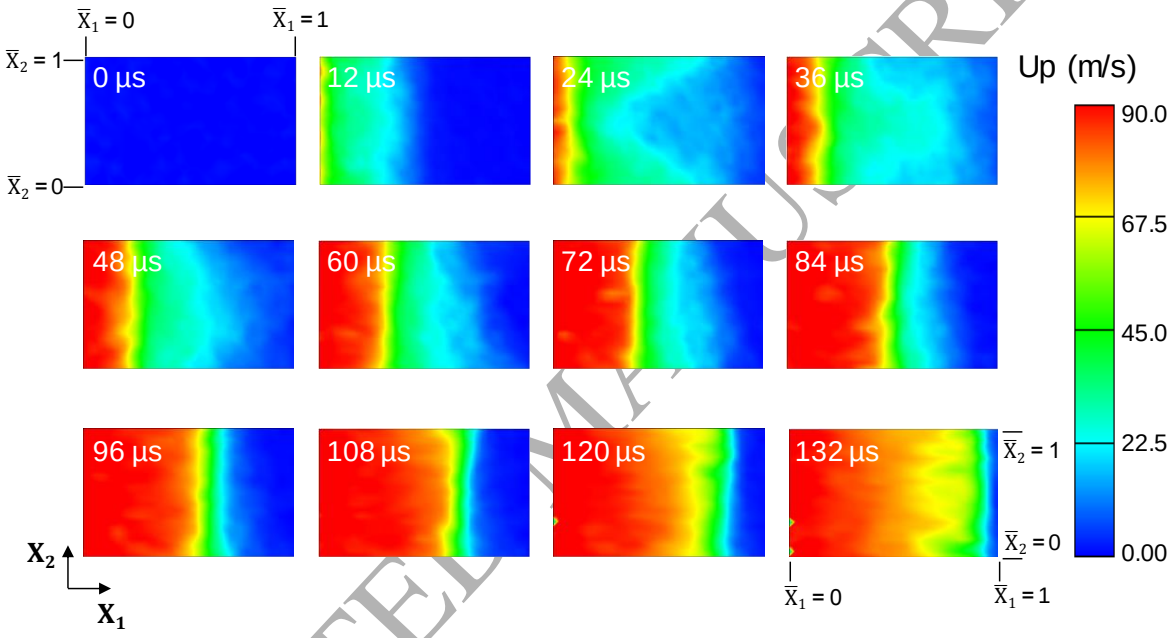

Fig. 8- Full-field particle velocity, U_p, maps at different times showing the propagation of a compaction front along the specimen axis.

Fig. 9 shows the velocity profiles extracted along $\overline{X}_2 = 0.5$. The data on this line, as discussed earlier, is considered to meet the uniaxial strain conditions required for the shock analysis. Temporal evolution of particle velocity extracted from different locations along the specimen axis shows an elastic precursor. The elastic precursor indicates that the location of the elastic wave front and shows a clear decay as the elastic wave transverses toward the distal end. Such behavior reduces the kinetic energy of the elastic wave and is possibly a result of cellular-scale

instability followed by cell-wall failure, and can be viewed as an energy dissipation mechanism in the examined foam. More discussions regarding the material response and possible mechanisms giving rise to superior energy absorption response of the examined material are provided in Sec. 4.4.

The elastic precursor is followed by a steep increase in the particle velocity magnitude that is indicative of compaction wave front location. It is clearly observed that the particle velocity increase due to the arrival of compaction wave occurs after a delay. The delay between the elastic precursor departure and the arrival of the compaction wave grows in time, as the location of interest moves toward the distal end. Therefore, the period of constant velocity expands over time for the points more closely associated with the distal end of the specimen. These observations are qualitatively similar to the previous plate impact study that has been performed in polyurethane foam (Zaretsky et al., 2012).

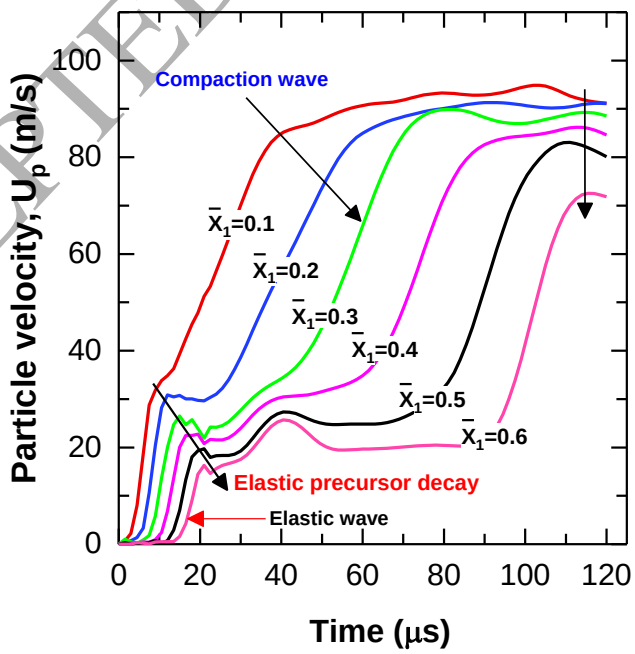

Fig. 9- Particle velocity with time at different axial locations. Elastic precursor, elastic wave and compaction wave are marked.

The particle velocity profile can be used to calculate the velocities of the elastic precursor (i.e. elastic wave speed) and the compaction wave front. The elastic wave front can be located in time by tracking the location of the maximum value of the particle velocity gradient (max $|dU_p/dx|$). This has been shown in Fig. 10a where the location of maximum velocity gradeint is found and marked. Plotting the variation of the location of elastic wave front in time, one can estimate the elastic wave speed of the examined material. Fig. 10b indicates the location of elastic precursor as a function of time. The slope of the best fitted line can be regarded as the elastic wave speed in the material. Accordingly, the elastic wave speed was calcualted as 740 m/s in this work. Interestingly, the theoretical elastic wave speed, c_L, assuming a uniaxial strain condition in the examined material was calculated as 730±80 m/s using Eq. 6:

$$c_L = \sqrt{\frac{(1-\upsilon_e)E}{(1-2\upsilon_e)(1+\upsilon_e)\rho_0}} \tag{6}$$

where E denotes the quasi-static elastic modulus of the material, measured as 49.2±4 MPa. ρ_0 is the initial density of the material (= 154±5 kg/m^3), and the parameter υ_e in Eq. 6 denotes the Poisson's ratio of the material in elastic deformation regime, independently measured in-house as 0.35±.01.

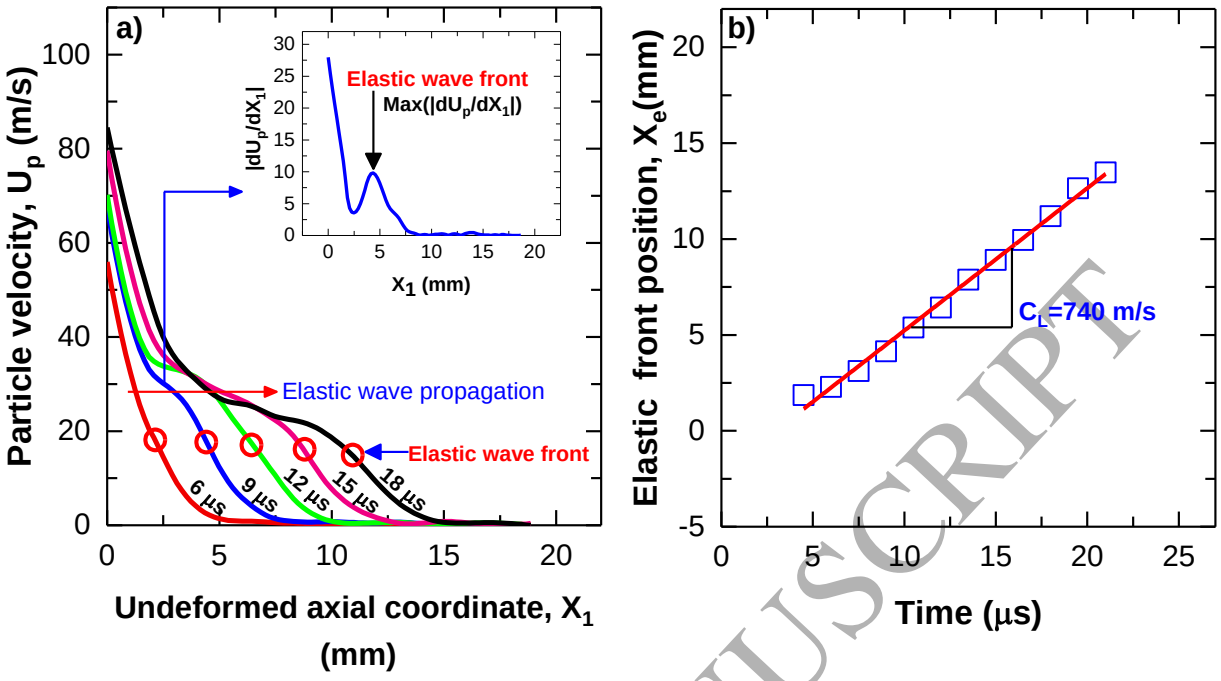

Fig. 10- (a) Spatial variation of particle velocity at different times, indicting the propagation of elastic wave through the specimen. (b) Elastic wave front location vs. time, used to estimate elastic wave speed.

Very similar to the approach used to estimate the location of elastic wave, compaction wave front can also be tracked in time using the maximum particle velocity gradient (max $|dU_p/dx|$). Fig. 11a shows the variation of particle velocity in space extracted at different times. Particle velocity at the impacted end of the specimen reaches a constant value when the complete compaction occurs at the impact face. The locations of maximum particle velocity gradients are marked on the curves. Comapring Fig. 10a with Fig. 11a, it is clearly seen that the elastic wave reaches the distal end at t = 24 µs, whereas the compaction wave front takes a significantly longer time to traverse the specimen length. The compaction wave velocity was estimated for the examined material as 139 m/s, the value of which is 5 times lower than the elastic wave speed in the specimen.

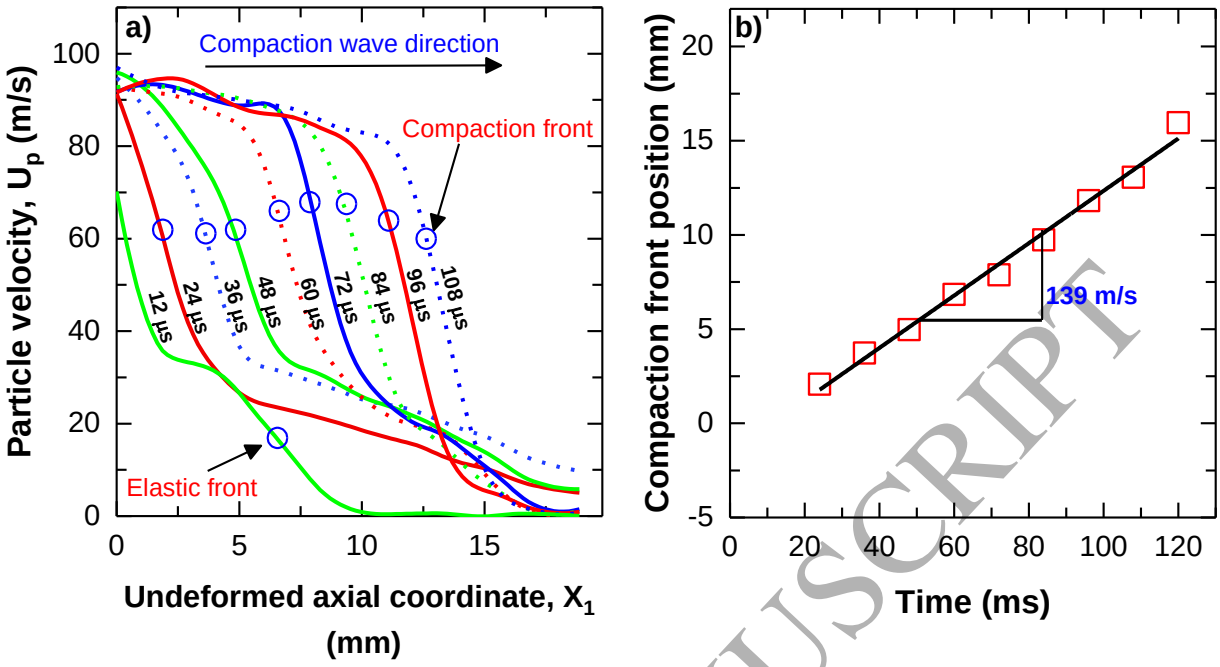

Fig. 11- (a) Spatial variation of particle velocity at different times, indicting the propagation of compaction wave through the specimen. (b) Compaction wave front location vs. time, used to estimate compaction wave speed.

The compaction wave speed is calculated for different impact velocities using similar procedure described in the previous section. Compaction speed at different impact velocities and at different particle velocities are shown in Fig. 12. In order to establish the repeatability of the measurements, two experiments are performed at an impact velocity close to 90 m/s. The compaction wave velocity was appeared to be very close, i.e within 7% variation.

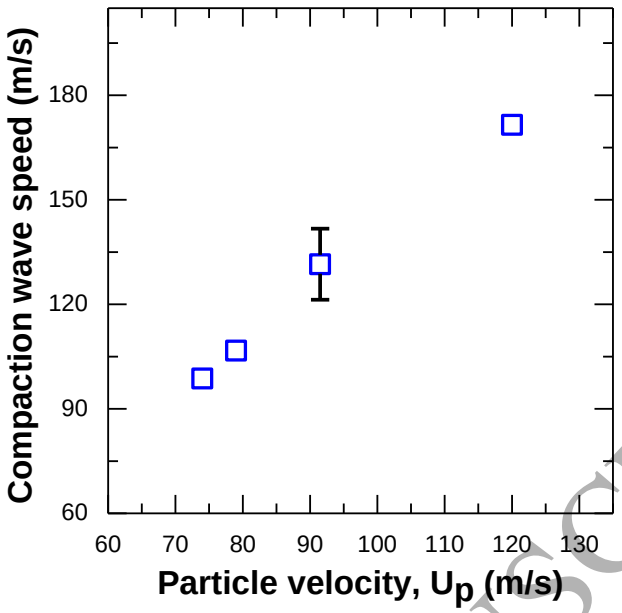

Fig. 12- Compaction wave speed at different particle velocities

4.3. Acceleration and Stress Calculations

The axial acceleration is calculated from the displacements field using Eq. 5. Spatial Distribution of axial acceleration is plotted in Fig. 13a for various times. The peak accelerations on each curve indicate the location of the stress wave front. For instance, considering the curve plotted for t = 24 μs, two local peaks can be identified. The first, having a larger magnitude, is indicative of the location of the compaction wave, while the second acceleration peak, closer to the distal end of the specimen, indicates the elastic wave location. Determination of elastic and inelastic wave speeds from the acceleration curves has been performed previously by Wang et al. (Wang et al., 2013), documented to be an accurate means to study and quantify wave propagation in an impacted specimen. Accordingly, one can track the acceleration peaks in time to analyze wave propagation and speed in the material. Such an analysis will not be conducted in this work, since wave speed analysis was already performed using particle velocity data in the previous section.

However, the significance of the acceleration curves in this work is highlighted here in terms of facilitating the study of wave propagation in both qualitative and quantitative manners:

Let us consider our impacted foam specimen again. Upon the establishment of the contact between the impactor and the specimen, an elastic stress wave is immediately formed at the impact end of the specimen and traverses along the axis with a speed of 740 m/s. The elastic wave band produces an elastic compression during its passage through the material. This elastic compression shows itself in the form of a local sudden increase in displacement of the particles exposed to the wave. The impulsive motion of the particle produces a significant local acceleration, indicated by a peak in the acceleration curves shown in Fig. 13a. Similar to the elastic wave, upon the formation and propagation of the compaction wave, material particles again experience an abrupt displacement increase, but this time with significantly larger amplitudes. Therefore, a second acceleration peak, indicative of the location of the compaction wave, is formed on the curves. The acceleration peak in this case is clearly shown to travel at a significantly lower pace, as discussed previously. Acceleration along with the initial density data obtained and discussed earlier can be used to calculate temporal and spatial distributions of inertia stress. Inertia stress fields can then be used to identify wave propagation behavior and the possibility of the occurrence of wave dispersion in the material. Fig. 13b depicts the distribution of inertia stress along specimen length at different times. The stress profile obtained at t =24 μs shows a two-wave structure, where an elastic wave precedes the propagation of the compaction wave. The two stress waves traverse along the axis of the specimen at different speeds. Reflection of the elastic wave from the distal end produces a compressive stress which is propagating in reverse direction.

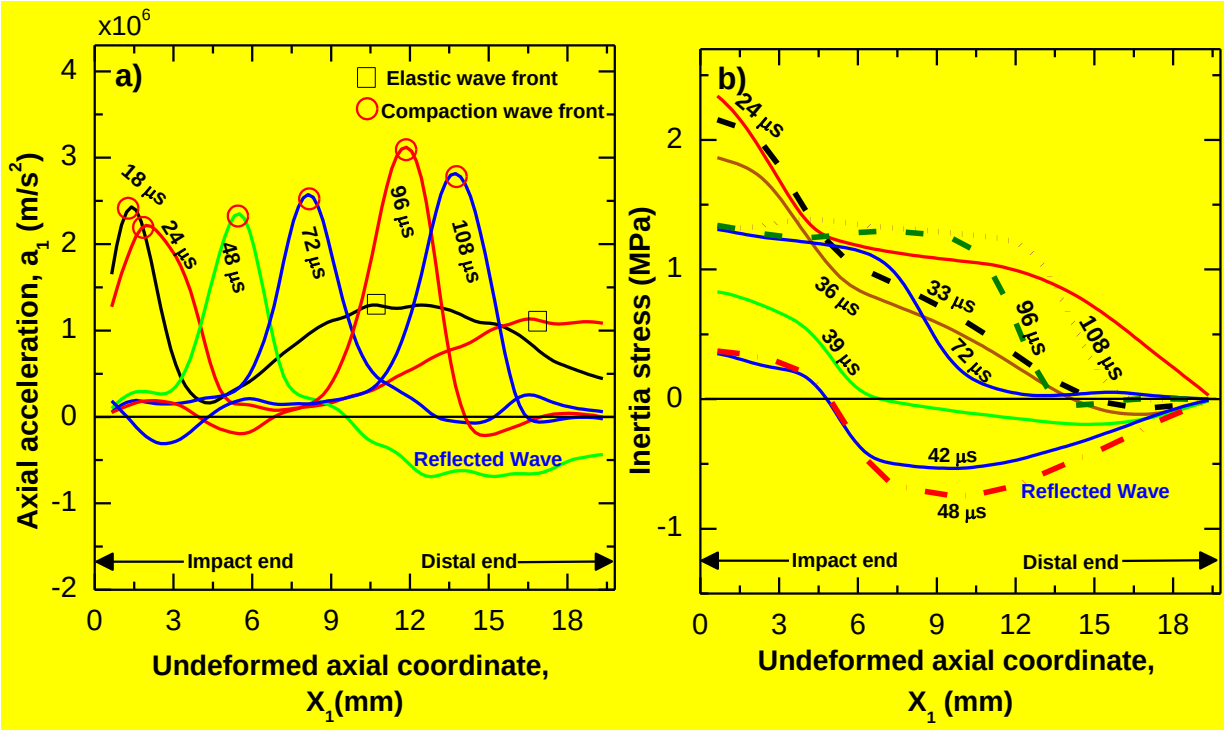

Fig. 13- a) Spatial variation of axial acceleration at different times. Locations of elastic and compaction waves are marked, b) spatial variation of axial inertia stress at different times.

It should be noted here, the eq.3 contains a boundary term ($P_{11}(0,t)$) and inertia stress term. The boundary term, ($P_{11}(0,t)$, is non-zero once the elastic wave reaches the distal end. In this study, however, only the inertia stress is calculated. Therefore, negative sign in the stress should not be seen as a tensile wave, as the total stress is the sum of boundary term and the inertial stress component. The negative sign indicates the reflected wave is compressive in nature but propagating in leftward direction. This wave essentially releases the inertial component of the stress, for instance see t=39, 42 48 and µs.

An X_1-t diagram, Fig 14, is plotted in order to explain the elastic precursor propagation and its reflections. It is shown that the elastic precursor first reflects at the distal end and propagates

towards the negative X_1 direction and then reflects back at the compaction front. To see the nature of reflections of the elastic precursor a strain time plot at three different spatial location is shown in Fig.14 b. At all the points considered, no release of strain is observed, supporting the reflection wave is compressive. For instance, at point C at the distal end of the sample axial strain increases to 0.1 due to multiple elastic reflections. Upon arrival of the compaction wave at t= 120 μs, the axial strain steeply increases. Damping of the elastic stress wave after multiple reverberations is observed and could due to the cellular scale failure in the material. A similar effects of elastic precursor reflections can be seen in (Harrigan et al., 2010).

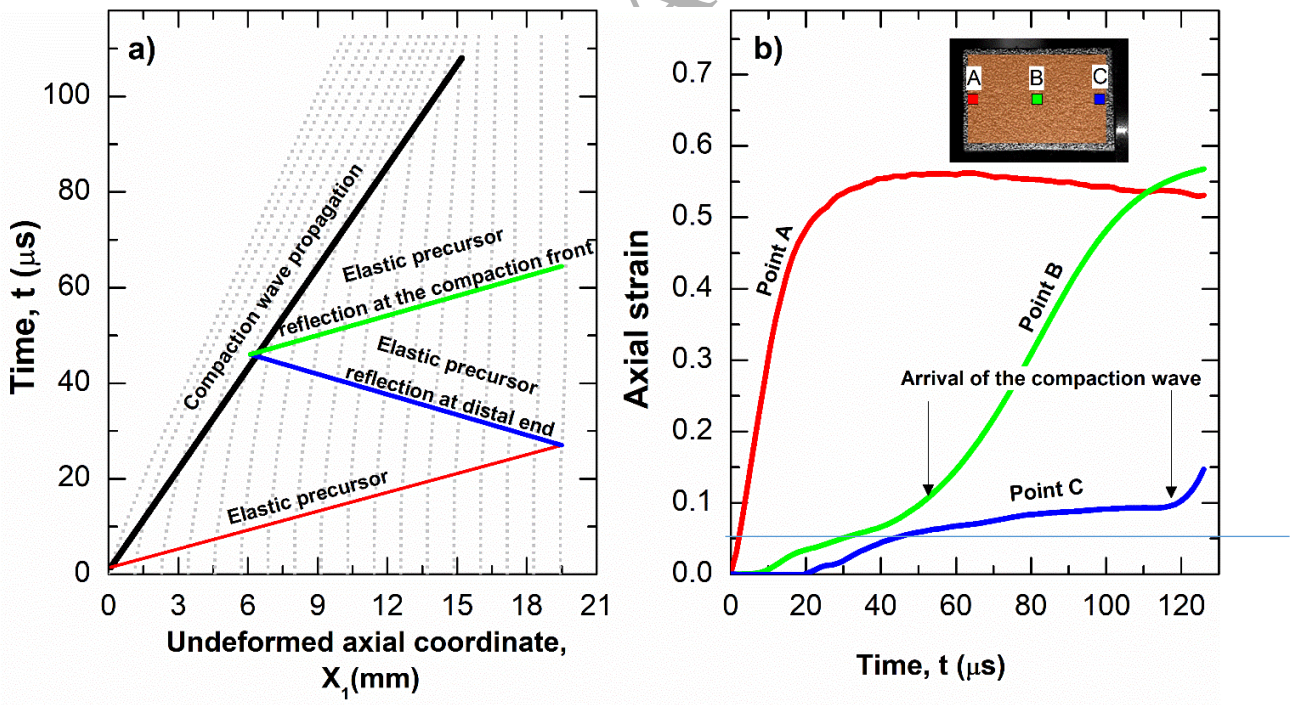

Fig. 14- a) X_1-t diagram shows the compaction wave front locations, elastic precursor and its reflection, b) variation of axial strain with time at different spatial locations.

In order to compare the estimated stress from the full-field measurements with the one-dimensional shock theory, the stress jump was calculated. Once the elastic wave reaches the distal end of the sample, it can be shown that the total stress at any point in the material is the sum of the stress due to the reaction force at the distal end and the inertia stress associated with the motion of particles (Koohbor et al., 2016c). Therefore, after elastic precursor reflects from the distal end and extenuates, the reaction force at the support stays approximately constant until the arrival of the compaction wave. The total stress that is estimated from the inertia stress calculation behind the compaction front will be equal to the stress jump across the compaction. Using the one-dimensional shock analysis and assuming a zero Poisson's ratio, the stress jump across the compaction front is given by (Li and Reid, 2006),

$$\sigma_1 - \sigma_2 = \frac{\rho_o (U_1 - U_2)^2}{\varepsilon_1 - \varepsilon_2} \tag{7}$$

Where, the $\sigma_1, U_1, \varepsilon_1$ and $\sigma_2, U_2, \varepsilon_2$ are stress, particle velocity and engineering strain behind and ahead of the compaction front (shock front), respectively. The particle velocities and strains were obtained from experiments. Using these quantities, the stress jump across the front is calculated using Eq. 7. Fig.15 shows the stress jump estimated from the inertia stress calculation and one-dimensional shock wave analysis for different particle velocities. The jump calculated from full-field measurements is very close to the stress estimated using one-dimensional shock wave equations.

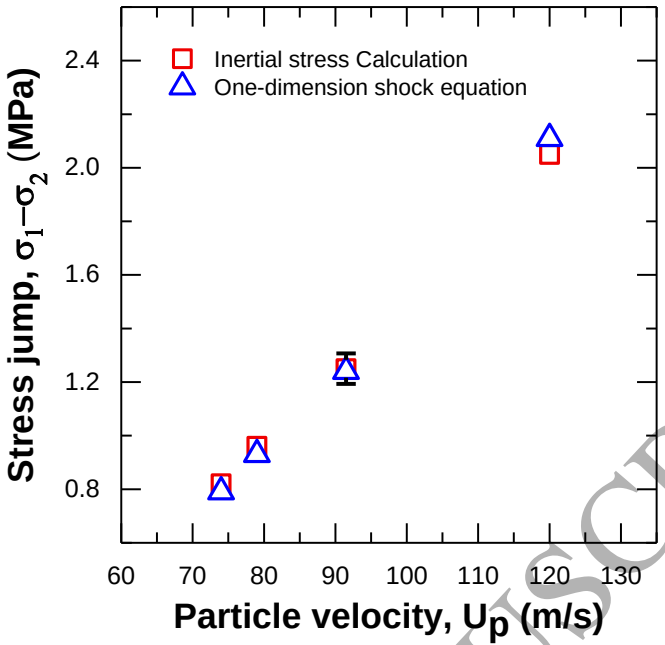

Fig. 15- Comparison of stress jump estimated from the experiments and the shock equations.

4.4. Compaction Wave Thickness and Dissipation Mechanisms

A brief discussion is presented in this section on the possible mechanisms attributing to the enhanced energy absorption and damping response of the examined material. First, we will focus on the study of compaction wave thickness and its evolution. In this regard, spatial gradients of stress at any given time during dynamic deformation can be used to estimate the thickness of the compaction wave. Compaction wave thickness, δ, can be simply determined using Eq. 8 (see Fig. 16a) (Gómez et al., 2012):

$$\delta = \frac{\sigma_1 - \sigma_2}{\max\left(\partial\sigma/\partial x\right)} \tag{8}$$

where σ_1 and σ_2 denote the stress magnitudes measured at impact and distal ends of the specimen, respectively. Note that stresses in Eq. 8 denote the total stress values; however, following the discussions provided earlier, the difference between the local stress values would be equal to the difference of the inertia stresses developed on the corresponding locations. Therefore, the inertia stress values determined earlier can be directly used in conjunction with Eq. 8 to approximately calculate the compaction wave thickness.

Considering the stress curves discussed earlier, variation of compaction wave thickness in time was obtained, as shown in Fig. 16b. It is clearly seen in Fig. 14b that the compaction wave is formed during the first 24 μs after the impact. Interestingly, a stable compaction wave propagation is observed after t = 24 μs which is devised with a constant compaction wave thickness close to 3±0.5 mm. However, several oscillations of the compaction wave thickness were observed that are due the interference of elastic and inelastic waves. Regardless of the local oscillations, compaction wave thickness remains constant for the entire duration of the deformation after t =24 μs. The unchanged thickness of the compaction wave indicates that the nonlinearities are balanced with the dissipation in the material showing a stable compaction wave propagation with constant velocity.

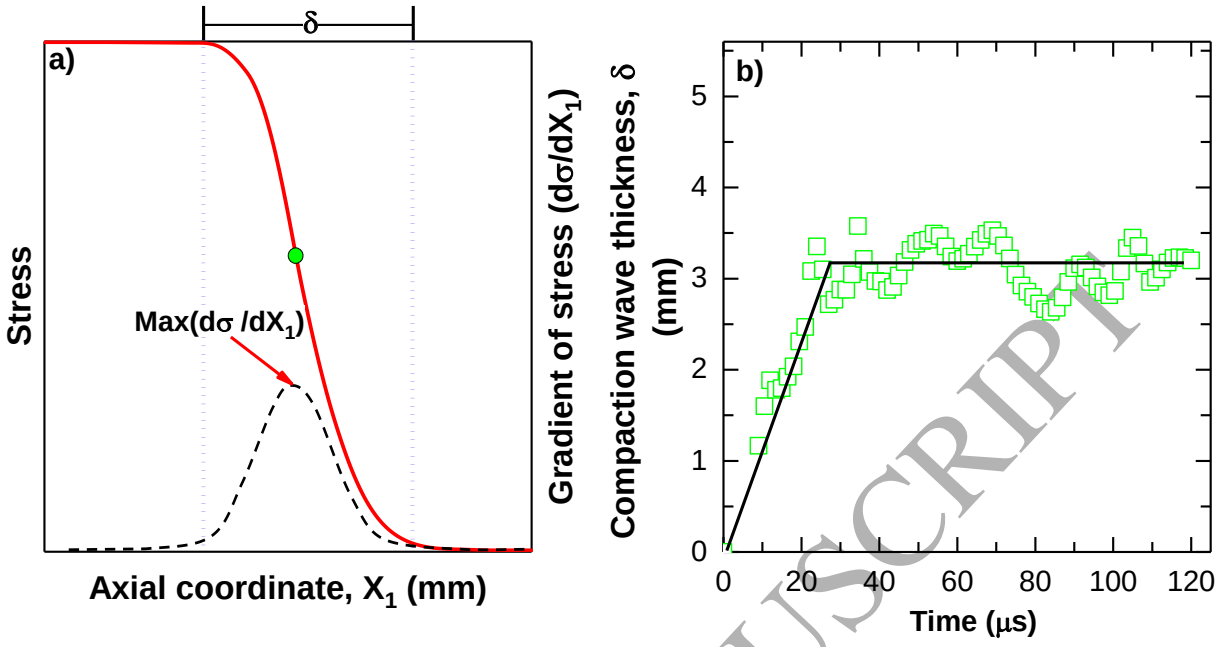

Fig. 16- (a) schematic spatial variation of stress used for approximation of the compaction wave thickness, and (b) variation of compaction wave thickness in time measured for the examined material.

Dissipation of the kinetic energy, on the other hand, is the principal mechanism contributing to the enhanced damping response of the examined foam. From the materials perspective, energy dissipation takes place following the cellular scale damage within the cell structure of the material. To provide a more in-depth insight on cellular-scale damage, we will adopt the simplified equations described in (Koohbor et al., 2017). Detailed derivation of the cellular-scale mechanisms is not within the scope of the present work but can be found elsewhere (Koohbor et al., 2017). It should only be emphasized that the assumption of idealized honeycomb structure is considered for the failure analyses and that the elastic modulus, yield stress and density of the parent solid polymer are assumed to be 385 MPa, 35 MPa, and 1200 kg/m^3, respectively. Using these values and assuming that the primary failure mechanisms for the foam specimen considered here are elastic buckling, plastic collapse and brittle failure (Koohbor et al., 2017), variation of

critical stress with respect to relative density can be plotted as shown in Fig. 17a. Note that the critical stress in Fig. 17a indicates the stress magnitude at which cellular scale failure takes place, and that the relative density is defined as the nominal density of the foam material, ρ_f, divided by the density of the parent solid polymer, ρ_s. Considering the curves shown in Fig. 17a, for the case of a closed-cell foam of 154 kg/m^3 nominal density with perfect hexagonal cellular structure, made from 1200 kg/m^3 polyurethane, cellular scale failure can occur at stress levels as low as 0.2 MPa. An evidence for such response is provided in Fig. 17b, where cellular scale images of the examined foam at initial and elastically deformed states are compared. It is clearly seen that the application of a nominal global stress of ≈1.8 MPa has resulted in the development of cellular-scale failure in the form of elastic buckling at multiple locations, particularly over the cell walls with relatively thinner sections. Such a low stress level is well below the apparent yield stress and crushing stress of the foam, but is shown to have been large enough to cause damage in the material. Such low stress magnitudes can be readily developed in the material during the elastic wave propagation time and may give rise to the variations in the cell structure of the material, consequently promoting the dissipation of the kinetic energy in the material.

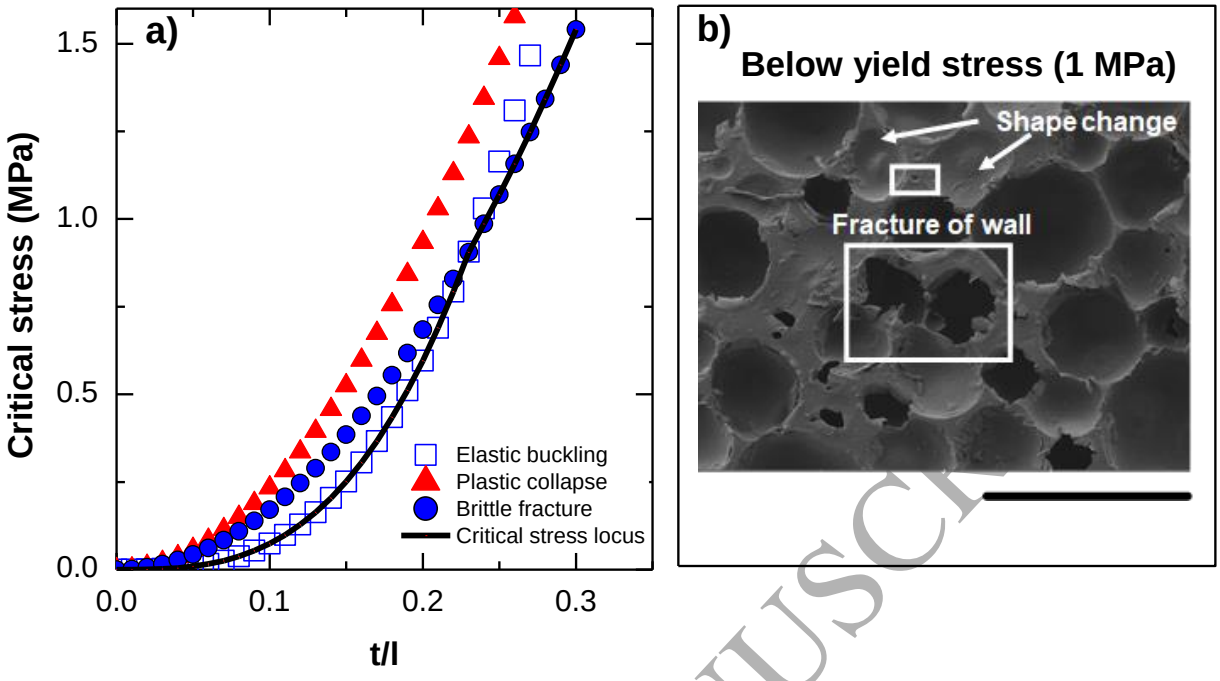

Fig. 17- a) Variation of critical stress with respect to relative density for three most probable failure mechanisms at cellular scales: elastic buckling, plastic collapse and brittle failure, b)

4.3. Critical impact velocity to generate shock

In order to identify the critical impactor velocity required for shock propagation, series of experiments at impact velocity range from 36 to 120 m/s are conducted. Interestingly, the deformation features for impact velocity bellow 57 m/s are distinctly different from the axial strain field that was seen in the case of compaction wave propagation discussed in section 4.1. Fig.18a shows the spatial axial strain profile for five different impact velocities at the time the projectile moves 6 mm in X1 direction after in contact with the specimen. As shown in the figure, as the impactor velocity increases, the corresponding strain near the impact end increases even though the projectile displacement remain the same. At impact velocity, Vi=57 m/s, the strain near the impact end is close to 0.43, slightly below the densification strain of the sample. Another strain peak is also seen near the distal end of the sample. When the impact velocity

increases from 57-62 m/s, the localization of the strain close to the distal end reduces and strain at the impact end increases to 0.49, very close to the densification strain of the sample. At impact velocity above 62 m/s, the strain at the impact end remain almost the same until it reaches 120/ms where the strain further increased by 20 %. Therefore, velocity between 57-62 m/s can be considered as a critical velocity for the transition to shock wave. It should be note here that the strain at velocities bellow 57 m/s is observed to be very small but not include in the plot to minimize the crowd in the plot. In order to confirm the observations, a spatial stress profile as a function of impact velocity before the elastic precursor reaches the support end of the sample is considered as shown in Fig.18b. Interestingly, the peak stress at the impact end of the sample for impact velocity, Vi=57 m/s, is 1.68 MPa, slightly below the quasi-static yield stress of the sample. Whereas at impact velocity Vi=62 m/s, the stress at the impact end is close to 2 MPa, which is above the yield stress of the foam material investigated in this study. It is well known that, a shock wave formed when the applied stress is higher than the flow stress of the material. Therefore, velocity between 57-62 m/s can be considered as the critical velocity required to generate shock wave in the foam material investigated in this study. In addition, when Vi increase from 62-120 m/s, the stress at the impact end increases from 2-4 MPa indicating a stronger shock wave propagation due to high amount of energy imparted due to impact.

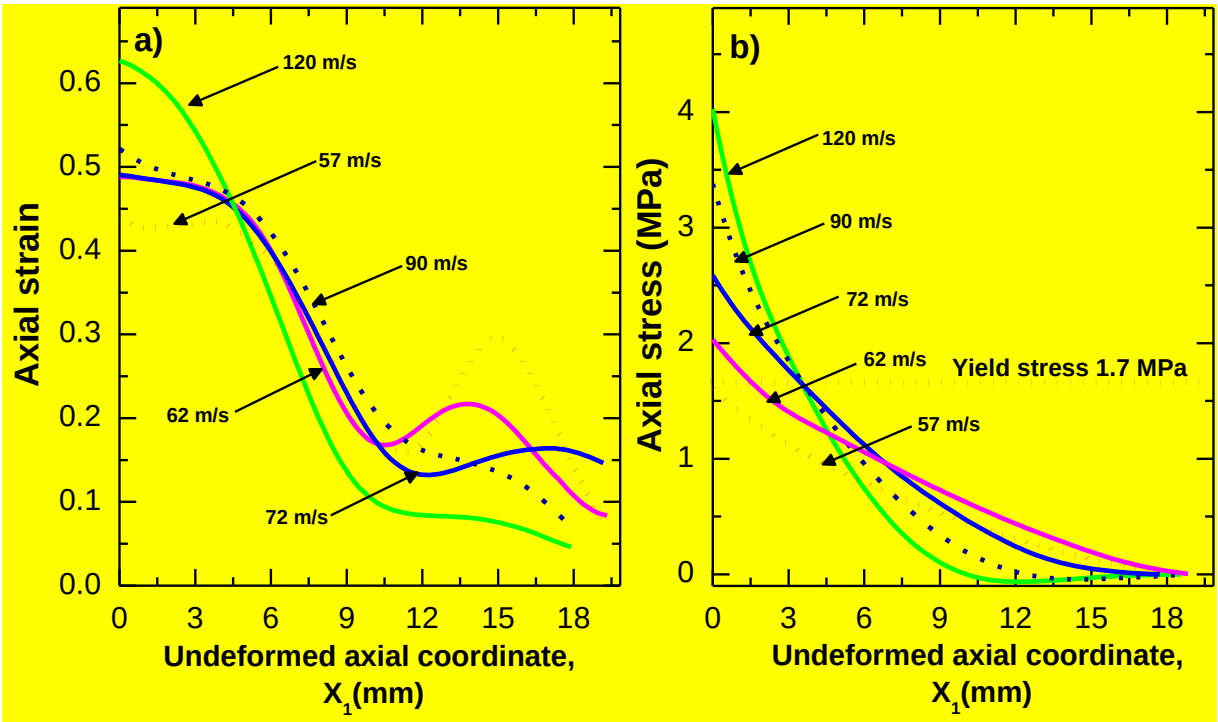

Fig. 18- Spatial axial strain and stress fields as a function of impact velocities along the length of the specimen.

5. Conclusion

An experimental setup based on ultrahigh speed imaging and digital image correlation is developed to understand the compaction wave formation and its propagation along the specimen. Projectile impact experiments at various impact velocities were conducted to generate compaction wave in a low density polymeric foam. The images are captured with the help of ultra-high-speed camera. The displacement field, strain field, particle velocity and acceleration fields are calculated from the DIC analysis of the images obtained from high speed photography. The spatial inertia stress field is calculated, and the time evolution of the compaction wave front thickness is estimated, for the first time, from displacement field obtained from DIC. The key observations of the experiments are,

- An elastic precursor was formed upon impact, and it propagated from the impact end to distal end at a velocity of 740 m/s for impact velocity of 90 m/s. The analytically calculated longitudinal sound velocity and the experimentally observed precursor velocity was in good agreement. Interestingly, a decay in the elastic precursor amplitude was noticed during its motion towards the distal end. This elastic precursor decay could be due to the cellular scale wall fracture and bending of thin walls during the elastic wave propagation.
- A compaction wave was formed followed by the precursor initiation and it traveled across the specimen at relatively low velocity. Therefore, before the plastic compaction wave reaches the impact end, the reflected elastic wave interacts with the plastic compaction wave. The stress jump across the compaction front is estimated from full-field displacement field and is compared with the one-dimensional shock theory. The estimated stress from the full-field measurement and the shock theory calculations are in good agreement.
- Compaction thickness was calculated to be 3±0.5 mm and it was constant after t=24 μs indicating a steady state compaction wave propagation in the material.

Acknowledgements

The financial support of Air Force Office of Scientific Research (AFOSR) under Grant No. FA9550-14-1-0209 is gratefully acknowledged. Todd Rumbaugh at Hadland Imaging LLC is gratefully acknowledged for providing high-speed camera used in this work.

References

Ashby, M.F., Evans, T., Fleck, N.A., Hutchinson, J.W., Wadley, H.N.G., Gibson, L.J., 2000. Metal foams: a design guide. Elsevier.

Barnes, A.T., Ravi-Chandar, K., Kyriakides, S., Gaitanaros, S., 2014. Dynamic crushing of aluminum foams: Part I–Experiments. Int. J. Solids Struct. 51, 1631–1645.

Deshpande, V.S., Fleck, N.A., 2000. High strain rate compressive behaviour of aluminium alloy foams. Int. J. Impact Eng. 24, 277–298.

Elnasri, I., Pattofatto, S., Zhao, H., Tsitsiris, H., 2007. Shock enhancement of cellular structures under impact loading : Part I Experiments 55, 2652–2671. doi:10.1016/j.jmps.2007.04.005

Gibson, L.J., Ashby, M.F., 1999. Cellular solids: structure and properties. Cambridge university press.

Gómez, L.R., Turner, A.M., Vitelli, V., 2012. Uniform shock waves in disordered granular matter. Phys. Rev. E 86, 41302.

Hanssen, A.G., Hopperstad, O.S., Langseth, M., Ilstad, H., 2002. Validation of constitutive models applicable to aluminium foams. Int. J. Mech. Sci. 44, 359–406.

Harrigan, J.J., Reid, S.R., Tan, P.J., Reddy, T.Y., 2005. High rate crushing of wood along the grain. Int. J. Mech. Sci. 47, 521–544.

Harrigan, J.J., Reid, S.R., Yaghoubi, A.S., 2010. The correct analysis of shocks in a cellular material. Int. J. Impact Eng. 37, 918–927.

Karagiozova, D., Langdon, G.S., Nurick, G.N., 2012. Propagation of compaction waves in metal foams exhibiting strain hardening. Int. J. Solids Struct. 49, 2763–2777.

Koohbor, B., Kidane, A., Lu, W.-Y., 2016a. Effect of specimen size, compressibility and inertia on the response of rigid polymer foams subjected to high velocity direct impact loading. Int. J. Impact Eng. 98, 62–74.

Koohbor, B., Kidane, A., Lu, W.-Y., 2016b. Characterizing the constitutive response and energy absorption of rigid polymeric foams subjected to intermediate-velocity impact. Polym. Test. 54, 48–58.

Koohbor, B., Kidane, A., Lu, W.-Y., Sutton, M.A., 2016c. Investigation of the dynamic stress–strain response of compressible polymeric foam using a non-parametric analysis. Int. J. Impact Eng. 91, 170–182.

Koohbor, B., Mallon, S., Kidane, A., Lu, W.-Y., 2015. The deformation and failure response of closed-cell PMDI foams subjected to dynamic impact loading. Polym. Test. 44, 112–124.

Koohbor, B., Ravindran, S., Kidane, A., 2017. Effects of Cell-Wall Instability and Local Failure on the Response of Closed-Cell Polymeric Foams Subjected to Dynamic Loading. Mech. Mater. doi:http://dx.doi.org/10.1016/j.mechmat.2017.03.017

Lee, S., 2006. Deformation rate effects on failure modes of open-cell Al foams and textile cellular materials 43, 53–73. doi:10.1016/j.ijsolstr.2005.06.101

Li, Q.M., Reid, S.R., 2006. About one-dimensional shock propagation in a cellular material. Int. J. Impact Eng. 32, 1898–1906.

Lopatnikov, S.L., Gama, B.A., Haque, M.J., Krauthauser, C., Gillespie, J.W., Guden, M., Hall, I.W., 2003. Dynamics of metal foam deformation during Taylor cylinder–Hopkinson bar impact experiment. Compos. Struct. 61, 61–71.

Merrett, R.P., Langdon, G.S., Theobald, M.D., 2013. The blast and impact loading of aluminium foam. Mater. Des. 44, 311–319.

Pattofatto, S., Elnasri, I., Zhao, H., Tsitsiris, H., 2007. Shock enhancement of cellular structures under impact loading : Part II analysis 55, 2672–2686. doi:10.1016/j.jmps.2007.04.004

Radford, D.D., Deshpande, V.S., Fleck, N.A., 2005. The use of metal foam projectiles to

simulate shock loading on a structure. Int. J. Impact Eng. 31, 1152–1171.

Ravindran, S., Koohbor, B., Kidane, A., 2016a. Experimental characterization of meso- scale deformation mechanisms and the RVE size in plastically deformed carbon steel. Strain.

Ravindran, S., Tessema, A., Kidane, A., 2017. Multiscale damage evolution in polymer bonded sugar under dynamic loading. Mech. Mater. 114, 97–106.

Ravindran, S., Tessema, A., Kidane, A., 2016. Note: Dynamic meso-scale full field surface deformation measurement of heterogeneous materials. Rev. Sci. Instrum. 87, 36108.

Ravindran, S., Tessema, A., Kidane, A., 2016b. Local Deformation and Failure Mechanisms of Polymer Bonded Energetic Materials Subjected to High Strain Rate Loading. J. Dyn. Behav. Mater. 2, 146–156.

Reid, S.R., Peng, C., 1997. Dynamic uniaxial crushing of wood. Int. J. Impact Eng. 19, 531–570.

Song, B., Forrestal, M.J., Chen, W., 2006. Dynamic and quasi-static propagation of compaction waves in a low-density epoxy foam. Exp. Mech. 46, 127–136.

Subhash, G., Liu, Q., Gao, X.-L., 2006. Quasistatic and high strain rate uniaxial compressive response of polymeric structural foams. Int. J. Impact Eng. 32, 1113–1126.

Sun, Y., Li, Q.M., McDonald, S.A., Withers, P.J., 2016. Determination of the constitutive relation and critical condition for the shock compression of cellular solids. Mech. Mater. 99, 26–36.

Sutton, M.A., Orteu, J.J., Schreier, H., 2009. Image Correlation for Shape, Motion and Deformation Measurements: Basic Concepts,Theory and Applications. Springer Science & Business Media.

Tan, P.J., Harrigan, J.J., Reid, S.R., 2002. Inertia effects in uniaxial dynamic compression of a closed cell aluminium alloy foam. Mater. Sci. Technol. 18, 480–488.

Wang, P., Pierron, F., Thomsen, O.T., 2013. Identification of material parameters of PVC foams using digital image correlation and the virtual fields method. Exp. Mech. 53, 1001–1015.

Zaretsky, E., Asaf, Z., Ran, E., Aizik, F., 2012. Impact response of high density flexible polyurethane foam. Int. J. Impact Eng. 39, 1–7.

Zhao, H., Elnasri, I., Abdennadher, S., 2005. An experimental study on the behaviour under impact loading of metallic cellular materials. Int. J. Mech. Sci. 47, 757–774.

Zheng, Z., Yu, J., Li, J., 2005. Dynamic crushing of 2D cellular structures: a finite element study. Int. J. Impact Eng. 32, 650–664.